




Adiabatic shear localization induced by rotationally accelerated shot peening

Yanfang Liu¹, Yang Cao^{1,*} , Wei Liu¹, Qingzhong Mao¹, Hao Zhou¹, Yonghao Zhao¹, and Yuntian Zhu^{1,2,*}

¹Nano and Heterogeneous Materials Center, School of Materials Science and Engineering, Nanjing University of Science and Technology, Nanjing 210094, China

²Department of Materials Science and Engineering, City University of Hong Kong, Kowloon, Hong Kong, China

Received: 8 October 2022

Accepted: 4 January 2023

Published online:

12 January 2023

© The Author(s), under exclusive licence to Springer Science+Business Media, LLC, part of Springer Nature 2023

ABSTRACT

Rotationally accelerated shot peening imposes high strain rates and strain accumulation on the surface of a pure nickel. As a result, a gradient structure is developed from the surface to the interior of the bulk sample. In addition to dislocation activities and deformation twinning, shear band is activated to accommodate localized shear strains at the outmost surface. A high density of defects accumulated during the strain hardening process is a prerequisite for the shear banding deformation. The orientation relationship between the deformed matrix and the shear bands, and thermally assisted mechanical rotation of nanograins occurred during partial dynamic recrystallization, together reveal the adiabatic nature of shear localization.

Introduction

In the last 30 years, gradient structures have attracted much attention due to their positive effects on various properties, such as tensile strength, fatigue strength, impact toughness and corrosion resistance for metallic materials [1–3]. Rotationally accelerated shot peening (RASP) is one of the surface severe plastic deformation (SPD) techniques that can induce gradient structures in the surface layers of metallic materials [4–6]. During RASP processing, the surface layer is repetitively deformed under multidirectional

impacts from rotationally accelerated shots. Both the strain rate and accumulated strain decrease with the increasing depth due to the absorption and dissipation of impact energy through depth, resulting in a significant grain refinement on the outmost surface and gradually decreasing densities of defects with increasing depth, namely the gradient structure [7].

The microstructural evolution and characteristic microstructures at different depths of the gradient structure are governed by deformation mechanisms, which have hence been studied extensively in the last decade [8–10]. Deformation mechanisms are affected by intrinsic factors including crystal structure,

Handling Editor: Ghanshyam Pilania.

Address correspondence to E-mail: y.cao@njust.edu.cn; y.zhu@cityu.edu.hk

stacking fault energy (SFE), grain size, and extrinsic factors including strain, strain rate and temperature [8, 11, 12]. For the materials with face-centered cubic (fcc) structures, dislocation slip and deformation twinning are the two major competing deformation mechanisms during the SPD-induced grain refinement processes [11]. Both dislocation slip and deformation twinning in general contribute to strain hardening and thus help sustaining uniform plastic deformation [11, 13, 14]. However, when the strain hardening rate can no longer catch up the increasing flow stress [13, 14] and/or when some sorts of work softening effects overwhelm, highly localized plastic deformation mechanisms such as shear banding can be activated [15–18]. According to studies [16, 18–21], shear bands usually form under high strain and/or high strain rate deformation. On one hand, shear bands may contribute to effective grain refinement in a highly localized manner [19–22], but on the other hand, shear bands are likely to lead the catastrophic failure of materials, unless special care is taken to effectively constrain the plastic instability [23]. While high strain and high strain rates are the characteristics of many surface-SPD techniques including RASP, surface mechanical attrition treatment (SMAT) [24] and surface mechanical grinding treatment (SMGT) [25], it is necessary to consider the effects of shear bands on the formation of gradient structures.

In this work, comprehensive experiments and analysis have been carried out to investigate the gradient structure and shear bands induced by RASP in pure nickel. Microstructural characterization of the shear bands in the gradient structure is conducted at different length scales, by electron back-scattered diffraction (EBSD) and transmission electron microscopy (TEM) analysis. The orientation relationship between the matrix and shear band is analyzed. The grain rotation occurred as a part of the dynamic recrystallization in shear band is revealed. At last, the shear bands as a contributing factor to the microstructural heterogeneity induced by RASP are discussed.

Material and methods

A commercial purity nickel (Ni, 99.3 wt%) was chosen as the model material. RASP was conducted at room temperature by using $\Phi 1$ mm GCr15 steel bearing balls with a shooting velocity of 70 m/s for

5 min, to create gradient structures on both sides of the Ni sample plate.

The microstructures of the samples were analyzed by EBSD and TEM. The samples for EBSD analysis were mechanically polished with 600, 800, and 1200 grit emery papers, subsequently fine polished to mirror finish with diamond paste, and finally polished to remove strained surface layer by using OP-U and OP-S suspensions. TEM samples were prepared by standard mechanical grinding and ion beam-thinned methods. EBSD analysis was performed using a Zeiss Auriga scanning electron microscope, with a step size of 40 nm. TEM analysis was performed with a TECNAI-G2-20-LaB6 microscope operating at 200 kV.

Results

Gradient structures

Figure 1 shows the microstructure of the as-received Ni sample. The sample has coarse grains with random orientations, and the average grain size is $\sim 120 \mu\text{m}$. Annealing twins are randomly observed, and the average twin thickness is $\sim 15 \mu\text{m}$. Figure 2 shows the gradient structures observed from two different regions (namely region 1 and region 2) on the same surface of the RASP Ni sample. At region 1, as shown in Fig. 2a, short and intermittent high angle grain boundaries (HAGBs, traced by black lines) are observed at the outmost surface layer within the

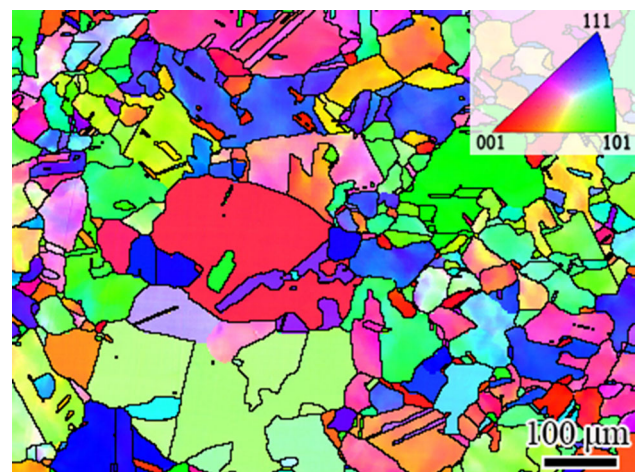


Figure 1 An EBSD map with the inverse pole figure (IPF) coloring scheme, showing the microstructure of the coarse-grained Ni sample.

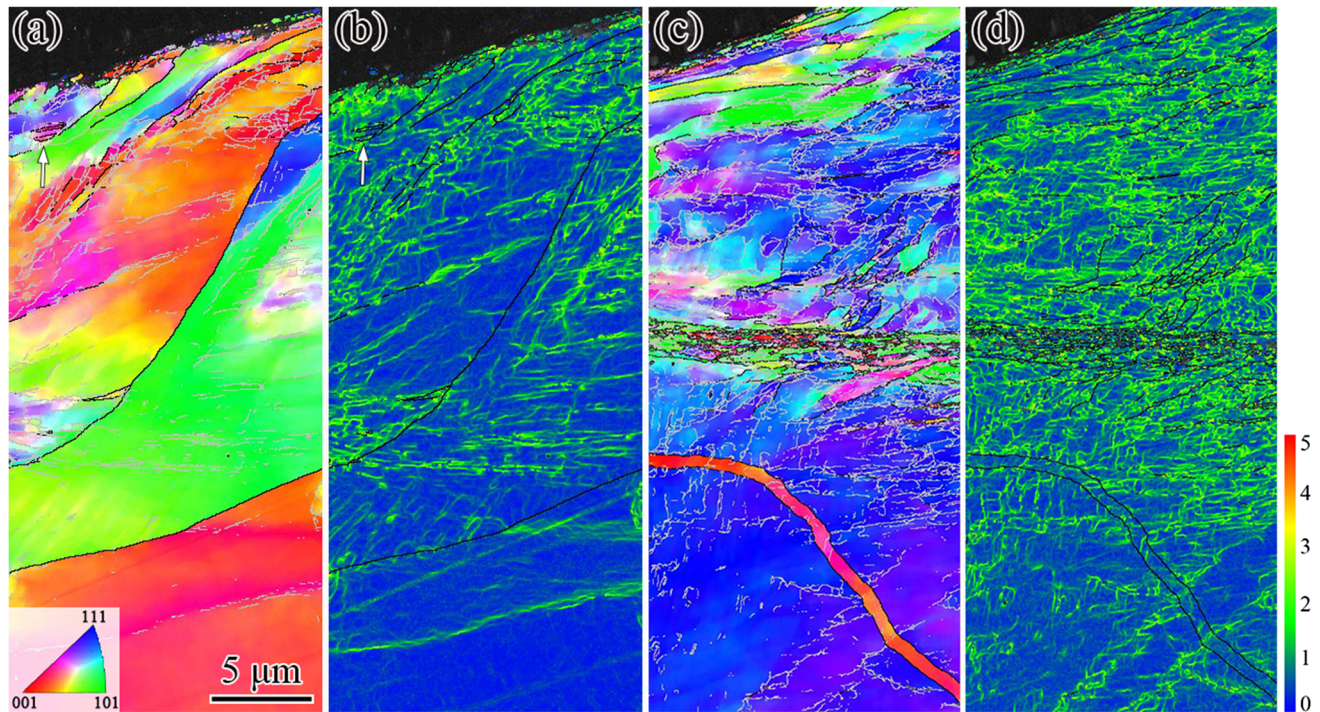


Figure 2 Typical IPF and KAM maps showing the gradient structure of the RASP sample. **a** The IPF map of region 1; **b** the KAM map corresponding to **a**; **c** the IPF map of region 2; **d** KAM map corresponding to **c**. (Twins are marked by white arrows.

HAGBs and LAGBs are traced by black and silver lines, respectively. The color code for KAM component is provided to the right of the figure).

depth of $\sim 1 \mu\text{m}$. These HAGBs are a result of severe plastic deformation-induced extreme grain refinement [6, 11, 26]. With increasing depth beneath the surface, the density of low angle grain boundaries (LAGBs, traced by silver lines) decreases, indicating that the plastic strain decreases. Figure 2b shows the Kernel average misorientations (KAM) measured in the gradient structure. KAM maps are commonly used to represent internal plastic strain build-up in a material [27–29]. In general, a higher KAM value (refer to the color code in Fig. 2) suggests a larger residual plastic strain, accommodated by a locally increased geometrically necessary dislocation (GND) density [23, 27]. As shown in Fig. 2b, the green and yellow segments agglomerate to form intermittent lines which mostly match the LAGBs shown in Fig. 2a, suggesting that high densities of GNDs have accumulated to form dislocation walls and LAGBs. The density of the segments with high KAM values is high at the outmost surface, and it decreases with the increasing depth, suggesting the gradient distribution of GND density through the depth. In addition, deformation twins marked by the white arrows (Fig. 2a, b) were generated due to the high strain and

strain rate at the outmost surface. Although it is on the same surface, the gradient structures observed at region 2 (Fig. 2c, d) are different from region 1: (1) The densities of HAGBs and LAGBs are higher in Fig. 2c than that in Fig. 2a; (2) an adiabatic shear band composed of ultrafine grains can be seen in the middle of Fig. 2c; and (3) the density of the segments with high KAM values is apparently higher in Fig. 2d than that in Fig. 2b. Provided that adiabatic shear bands are a result of localized high strain concentration which is usually induced by high strain rate deformation [20], region 2 evidently has experienced higher strain rate than region 1. Apart from the shear band, the densities of HAGBs, LAGBs and high KAM segments are significantly higher in region 2 than in region 1, indicating that region 2 has experienced significantly higher strain. Apparently, the strain and strain rate imposed by RASP is inhomogeneous across the sample surface, leading to inhomogeneous distribution of gradient structures. While shear bands and deformation twins have occasionally developed in the gradient structure, grain refinement in the gradient structure is mainly achieved by the grain subdivision mechanism involving the entanglement

of dislocations, the formation of dense dislocation walls (DDWs) and cell walls, transformation of DDWs and cell walls into LAGBs, and the evolution of LAGBs to HAGBs [30].

Shear banding

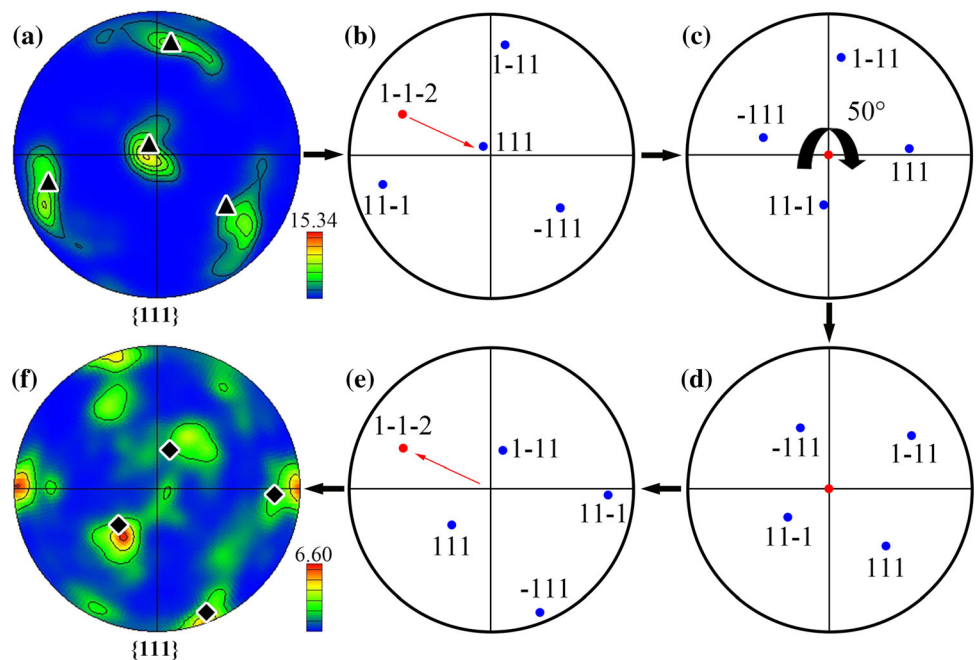
Stress and strain are highly concentrated in a shear band, leading to significant grain refinement and grain rotation inside the band [21]. As a result, specific orientation relationships are created between the fine-grained shear band and coarse-grained matrix [11, 31]. To reveal orientation relationship between the matrix and the shear band, {111} pole figures derived from the matrix region and the shear band region are shown in Fig. 3a, f, respectively. The normal to the cross section (Fig. 2c) of the RASP Ni sample corresponds to the centers of the pole figures (Fig. 3a, f). As shown in Fig. 3a, the {111} poles spread to form arcs of 50–60°; correspondingly, the majority of the boundaries in the matrix are LAGBs, and the misorientation angles between adjacent cells are low, as shown in Fig. 2c; hence, the overall large misorientation revealed in Fig. 3a is due to the accumulation of correlated LAGBs, rather than randomly scattered HAGBs. In other words, the matrix area shown in Figs. 2c and 3a is actually a strongly deformed single coarse grain containing a large number of LAGBs. Figure 3b–e shows the schematic

diagrams depicting 50° <112> rotation from the matrix to reach the texture of shear band. One grain containing a set of {111} planes is chosen for the demonstration of the rotation process, and the starting positions of the poles are shown in Fig. 3b. For the first step, the pole figure is shifted to have the $[1\bar{1}\bar{2}]$ pole placed to the center, and so the other poles are all shifted correspondingly, as shown in Fig. 3c. For the second step, the pole figure is rotated clockwise about the $[1\bar{1}\bar{2}]$ pole for 50° to reach the orientation as shown in Fig. 3d. For the last step, the $[1\bar{1}\bar{2}]$ pole is shifted to the starting position, and the other poles are shifted correspondingly to complete the rotation, as shown in Fig. 3e. Figure 3e matches well with the actual pole figure of Fig. 3f, indicating that the majority of the grains inside the shear band tend to have similar rotation routes, in this particular case 50° <112> rotation. Hence, shear banding has caused both grain refinement and grain rotation from the matrix grain.

Dynamic recrystallization

Another prevalent feature of the shear bands is that there are noticeable numbers of recrystallized grains having similar orientations but oriented away from the dominant texture. Most of the recrystallized grains are colored red and scattered inside the shear band, as shown in Fig. 2c and Supplemental Fig. S1.

Figure 3 a The contoured {111} pole figure derived from the matrix region in Fig. 2c (black triangles represent one representative set of {111} planes in the matrix); b–e sequential steps for the 50° <112> rotation that transforms the matrix to the textured shear band; (f) the contoured {111} pole figure derived from the shear band region (black lozenges represent the set of poles for the rotated grain in the shear band).

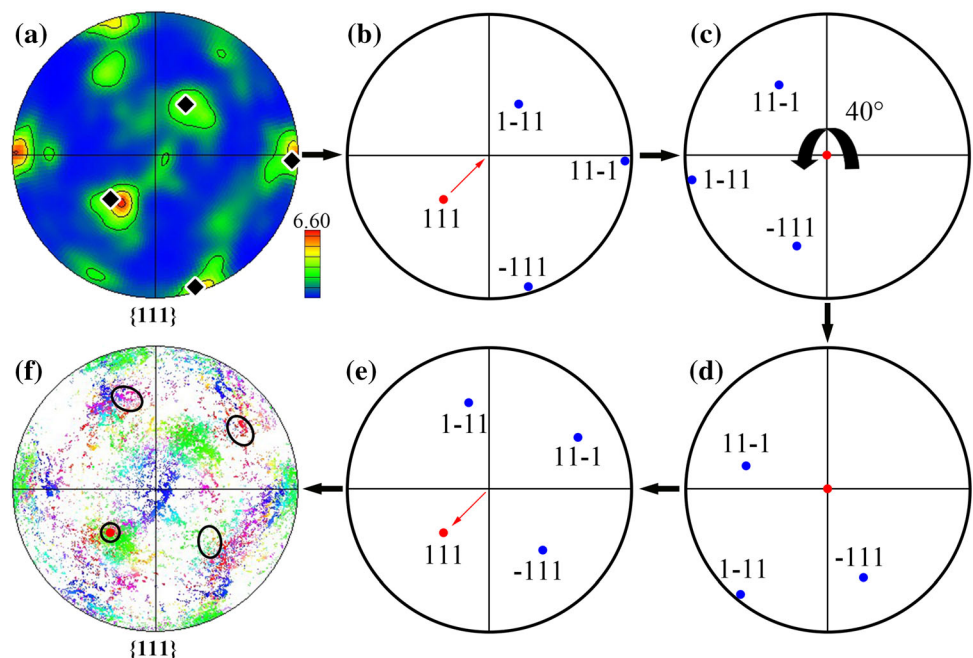


Systematic analysis reveals that most of the recrystallized grains have rotated 40° – 50° about the $[111]$ pole, as elucidated in Fig. 4. As an example of the analysis, a representative grain is chosen from inside of the shear band, and the corresponding poles are marked by black lozenges as shown in Fig. 4a. The set of poles shown in Fig. 4a is transformed to the schematic pole figure in Fig. 4b. This time the $[111]$ pole is chosen as the rotation axis and shifted to the center of the pole figure, as shown in Fig. 4c. The pole figure is rotated anti-clockwise about the $[111]$ pole for 40° to reach the orientation as shown in Fig. 4d. Then, the $[111]$ pole is shifted back to the starting position, as shown in Fig. 4e. By the same procedure, the chosen grain was rotated anti-clockwise about the $[111]$ pole for 40 – 50° , and the results fall into the regions enclosed by the ellipses in Fig. 4f. Apparently, the majority of the poles enclosed by the ellipses are red, as shown in Fig. 4f, corresponding to many of the recrystallized red grains observed inside the shear band shown in Fig. 2c. According to the literature [32, 33], transformation of the $S\{123\} \langle 634 \rangle$ texture to the $\text{cube}\{100\} \langle 001 \rangle$ texture by ~ 40 – $50^\circ \langle 111 \rangle$ rotation is common during static recrystallization of deformed fcc alloys. Therefore, it implies that thermally assisted recrystallization has occurred inside the shear band.

Heterogeneous deformation

A shear band beneath the RASP surface is captured by TEM, as shown in Fig. 5. This shear band has a width of less than $1 \mu\text{m}$, as shown in Fig. 5a. Outside the shear band, ultra-fine grains with an average grain size of $\sim 430 \text{ nm}$ have been achieved due to dislocation accumulation, as shown in Fig. 5b. However, the ultrafine grains are delineated by blurred boundaries, indicating that grain refinement is still ongoing without any noticeable recovery [11]. As shown in the inset in Fig. 5b, only a limited number of diffraction spots are visible, suggesting that the grain sizes are comparatively large in the region outside the shear band. In contrast, the sizes of the grains inside the shear band have been significantly refined to an average size of $\sim 170 \text{ nm}$, as shown in Fig. 5c. The randomly orientated nanograins inside the shear band contribute to the formation of the well-developed diffraction rings shown in the inset in Fig. 5c. Figure 6a clearly shows some nanograins as small as 20 nm (marked by arrows) in the shear band. A nanotwin is seen in the nanograin with a size of $\sim 100 \text{ nm}$. It has been reported that the conventional twinning mechanism involving fault-pairs may cease to operate due to the lack of mobile dislocations inside nanograins [34], and thereby, the nanotwin has to form by emission of Shockley partials from the grain boundary [35]. Since high temperature

Figure 4 **a** The contoured $\{111\}$ pole figure derived from the shear band region in Fig. 2c (black lozenges represent a set of poles for a grain in the shear band); **b**–**e** sequential steps for the $40^\circ \langle 111 \rangle$ rotation of a grain as a part of the dynamic recrystallization process; **f** the $\{111\}$ pole figure derived from the shear band region (black circles and ellipses enclose a set of poles for the recrystallized grains in the shear band).



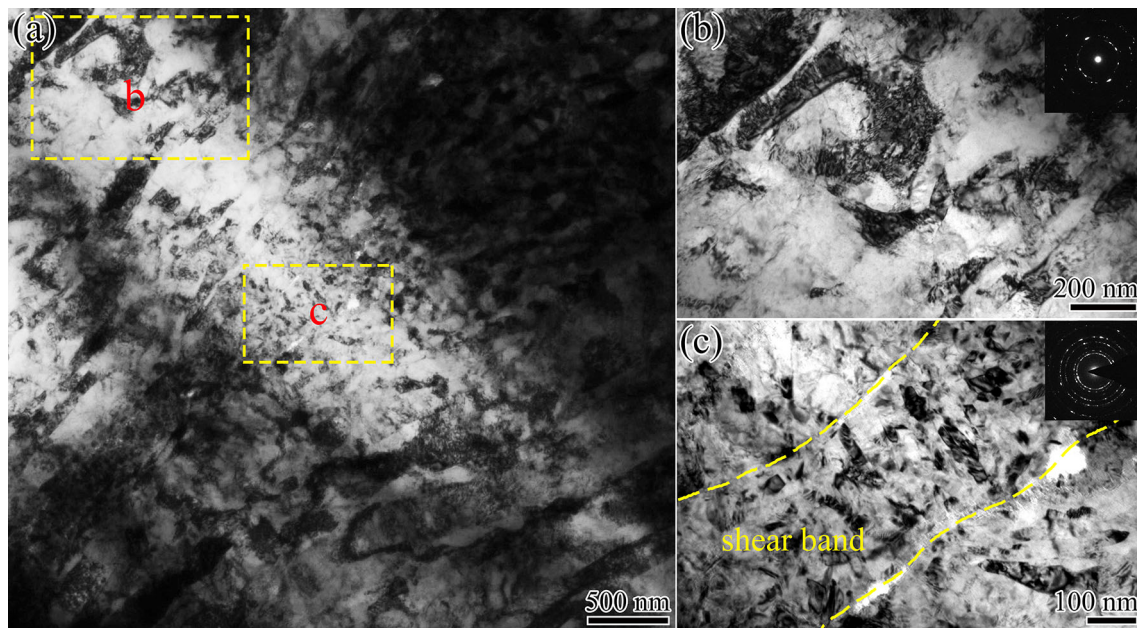


Figure 5 **a** A low-magnification TEM image showing an adiabatic shear band cutting across the gradient structure in the surface layer of the RASP Ni sample; **b** a magnified TEM image of the area marked “b” in **a**, showing ultrafine grains; **c** a magnified

TEM image of the area marked “c” in **a**, showing the adiabatic shear band containing nanograins (the same selected-area aperture was used to take selected-area electron diffraction patterns from the shear band and the region outside the shear band).

suppresses deformation twinning, the existence of nanotwins inside the shear band indicates that the temperature raise due to adiabatic heating may not be very high. In contrast, deformation twins have also been observed in coarse grains outside of the shear band, as shown in Figs. 2a and 6b. As shown in Fig. 6b, some of the twins have detached from the grain boundary, suggesting that the twins have nucleated at the grain interior by the conventional twinning mechanism. Provided that twinning in nanograins requires significantly higher stress than twinning in coarse grains, different twinning mechanisms found between inside and outside of the shear band in the same surface layer indicate significant heterogeneous deformation occurred due to the shear banding [34, 35].

Discussion

Adiabatic shear localization

It has been well established that adiabatic shear banding is the highly localized deformation governed by a complex function of strain, strain rate and temperature [15, 20]. As shown in Figs. 2d and 5a, high densities of defects including both tangled

dislocations and dislocation substructures have accumulated at the surroundings of the shear bands. The GND density deduced from the area outside the shear band in Fig. 2d is $\sim 1.43 \times 10^{15} \text{m}^{-2}$ which is higher than the GND density of $\sim 0.97 \times 10^{15} \text{m}^{-2}$ deduced from Fig. 2b. This result indicates that a high density of dislocations caused by strain accumulation is a prerequisite for adiabatic shear banding and thus agrees with the concept of dislocation pile-up avalanche model for adiabatic shear banding [36]. Under repetitive impacts by RASP, strain continuously accumulates on the surface layer of the Ni sample, resulting in the accumulation of defective structures including dislocation forests, dislocation cells, microbands and sub-grain boundaries, which provide barriers against dislocation motion [21, 37]. A sudden collapse of these barriers, namely dislocation avalanche, ultimately leads to the adiabatic shear localization in the form of a shear band.

The strain rate at the outmost surface layer is estimated to be 10^3 – 10^4 s^{-1} based on the theoretical model for ball–plate dynamic indentation [38]. Provided that deformation twins were absent in the pure Ni deformed at the strain rates of 10^2 – 10^3 s^{-1} [39], the observation of deformation twins in Fig. 6b also justifies that a high strain rate of at least 10^4 s^{-1} was

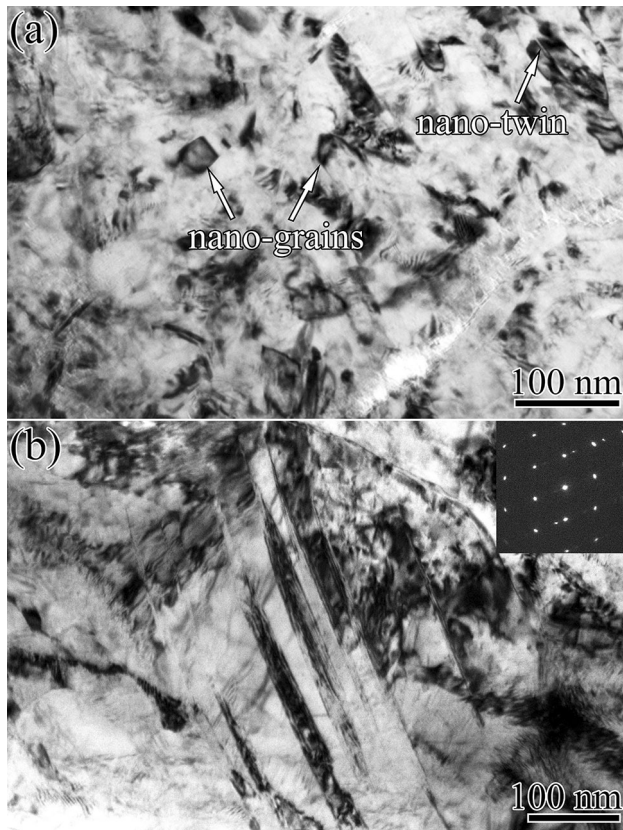


Figure 6 TEM images showing **a** nanograins and nanotwins observed inside a shear band; **b** deformation twins found outside the shear band.

achieved at the outmost surface of the RASP sample. The high strain rate on one hand accelerates the rate of dislocation generation, and on the other hand provides the momentum and stress required to trigger the nucleation of shear band [21, 36]. Once the shear band is nucleated, further straining will mainly concentrate in the shear band, leaving surrounding areas being strained at a much slower rate, resulting in fast expansion and propagation of the shear band. Meanwhile, strain concentration and high strain rate in the shear band elevate the local temperature in the blink of an eye, demonstrating the adiabatic nature [10, 21, 40]. Provided that the shear banding process is usually very fast, three orders of magnitude higher than the externally imposed strain rate [22, 41], the period for adiabatic heating and cooling in the shear band is extremely short [21]. Nevertheless, the temperature raise may not be high enough to drive full-scale diffusional recrystallization, evidenced by deformed grains with non-equilibrium GBs including the one containing a nanotwin as shown in Fig. 6a.

Therefore, in addition to the heating and cooling process, local stress and stored energy (in the form of dislocation substructures and vacancies) will also contribute to the dynamic recrystallization. Consequently, recrystallized grains tend to nucleate randomly from highly misoriented dislocation cells [16] rather than from migration of HAGBs [42]. Nevertheless, according to the literature [16, 21], diffusion during the cooling of the adiabatic shear band accounts for variations in the total angles of rotation of the recrystallized grains, explaining the reason for the $\sim 40\text{--}50^\circ$ $\langle 111 \rangle$ rotation of the recrystallized grains elucidated in Fig. 4.

Microstructural heterogeneity in the gradient structure

An ideal gradient structure is constituted of grains with significantly varied sizes, but configured to a gradient distribution of grain size [24, 43]. As a result, the nanostructured layers provide high strength and the coarse-grained core provides decent ductility. There is essentially a transition region in-between the nanostructures and coarse-grained structures to accommodate the incompatibility induced due to significantly different plastic behaviors occurred concurrently, by generating and trapping a high density of extra GNDs [5, 24]. Such a strong strain incompatibility in a narrow region is the source of the beneficial hetero-deformation-induced hardening effects, if the transition region is well sandwiched/constrained by the high strength nanostructured layer and the ductile coarse-grained core. However, an adiabatic shear band cutting through the gradient structure as shown in Figs. 2c and 5 strongly distorts the ordered configuration, creating an additional microstructural heterogeneity and local stress concentration sites along the shear band. Although there has not been any literature to-date to report that shear bands deteriorate the mechanical properties of bulk samples, many gradient-structured materials have not shown outstanding combinations of strength and ductility either as theoretically predicted [24, 44–48]. It is suspected that large shear bands will be preferred crack nucleation sites during plastic deformation of the gradient-structured materials and thus deteriorate the overall mechanical properties. While shot-peening-based methods such as RASP and SMAT are often used for making gradient structures, careful conduct of experiments is

necessary to avoid or minimize the negative effects of shear bands. Notwithstanding, the effects of shear bands for grain refinement cannot be overlooked. Therefore, we propose two ways for minimizing the negative effects of shear bands: (1) disperse the shear bands in the nanostructured region and prevent the penetration of the shear bands to the transition region; (2) avoid the formation of shear bands by imposing uniform strain accumulation across the specimen surface.

Conclusions

Gradient structure has been formed on a Ni sample by RASP processing. While the high strain and strain rate imposed by RASP caused significant grain refinement at the outmost surface layers, shear bands have also formed randomly due to non-uniform local stress and strain concentrations. Detailed EBSD analysis reveals that the $50^\circ \langle 1\bar{1}2 \rangle$ rotation route is an important part of the grain refinement process that occurred during shear banding. Adiabatic heating, high local stress and stored energy contribute together to drive partial dynamic recrystallization. The recrystallized grains are usually as small as a few tens of nanometer and demonstrate further $\sim 40\text{--}50^\circ \langle 111 \rangle$ rotation from the deformed nanostructure in the shear band. EBSD and TEM results show that high densities of defects are the prerequisite for adiabatic shear banding, supporting the dislocation pile-up avalanche model. Although shear banding is effective for grain refinement, large shear bands cutting across the gradient-structured layers introduced an additional heterogeneity which may act as local stress concentration sites and even preferred sites for crack initiations.

Acknowledgements

This work is supported by the National Natural Science Foundation of China (Grant No. 51931003, 52071181 and 51971112), the Natural Science Foundation of Jiangsu Province (Grants No BK20220962) and the Fundamental Research for the Central Universities (No. 30919011405). The authors are thankful for the technical support from Jiangsu Key Laboratory of Advanced Micro & Nano Materials

and Technology, and Center of Analytical Facilities Nanjing University of Science and Technology.

Declaration

Conflict of interest The authors declare that they have no conflict of interest.

Ethical approval This article contains no animal or human studies conducted by any of the authors.

Supplementary Information: The online version contains supplementary material available at <http://doi.org/10.1007/s10853-023-08152-9>.

References

- [1] Liu XC, Zhang HW, Lu K (2013) Strain-induced ultrahard and ultrastable nanolaminated structure in nickel. *Science* 342:337–340. <https://doi.org/10.1126/science.1242578>
- [2] Huang HW, Wang ZB, Lu J, Lu K (2015) Fatigue behaviors of AISI 316L stainless steel with a gradient nanostructured surface layer. *Acta Mater* 87:150–160. <https://doi.org/10.1016/j.actamat.2014.12.057>
- [3] Song D, Ma A, Sun W, Jiang J, Jiang J, Yang D, Guo G (2014) Improved corrosion resistance in simulated concrete pore solution of surface nanocrystallized rebar fabricated by wire-brushing. *Corros Sci* 82:437–441. <https://doi.org/10.1016/j.corsci.2014.01.034>
- [4] Wang XLYS, Zhang Q, Zhao YH, Zhu YT (2017) Gradient structured copper by rotationally accelerated shot peening. *J Mater Sci Technol* 33:758–761. <https://doi.org/10.1016/j.jmst.2016.11.006>
- [5] Liu Y, Cao Y, Zhou H, Chen X, Liu Y, Xiao L, Huan X, Zhao Y et al (2020) Mechanical properties and microstructures of commercial-purity aluminum processed by rotational accelerated shot peening plus cold rolling. *Adv Eng Mater* 22:1900478. <https://doi.org/10.1002/adem.201900478>
- [6] Liu Y, Zang Y, Cao Y, Liu W, Mao Q, Zhou H, Jiang W, Zhao Y et al (2021) Significance of surface layer integrity for sustaining the ductility of gradient-structured nickel. *Mater Lett* 303:130491. <https://doi.org/10.1016/j.matlet.2021.130491>
- [7] Lu K, Lu J (2004) Nanostructured surface layer on metallic materials induced by surface mechanical attrition treatment. *Mater Sci Eng A* 375–377:38–45. <https://doi.org/10.1016/j.msea.2003.10.261>
- [8] Hasan MN, Liu YF, An XH, Gu J, Song M, Cao Y, Li YS, Zhu YT et al (2019) Simultaneously enhancing strength and ductility of a high-entropy alloy via gradient hierarchical

- microstructures. *Int J Plast* 123:178–195. <https://doi.org/10.1016/j.ijplas.2019.07.017>
- [9] Wu XL, Yang MX, Yuan FP, Chen L, Zhu YT (2016) Combining gradient structure and TRIP effect to produce austenite stainless steel with high strength and ductility. *Acta Mater* 112:337–346. <https://doi.org/10.1016/j.actamat.2016.04.045>
- [10] Bahl S, Suwas S, Ungár T, Chatterjee K (2017) Elucidating microstructural evolution and strengthening mechanisms in nanocrystalline surface induced by surface mechanical attrition treatment of stainless steel. *Acta Mater* 122:138–151. <https://doi.org/10.1016/j.actamat.2016.09.041>
- [11] Cao Y, Ni S, Liao X, Song M, Zhu Y (2018) Structural evolutions of metallic materials processed by severe plastic deformation. *Mater Sci Eng R* 133:1–59. <https://doi.org/10.1016/j.mser.2018.06.001>
- [12] Zhang J, Cao Y, Gao H, Yang X, Shu B, Zhu Y, Sharma B, Ameyama K et al (2020) Influence of strain rate on mechanical behaviours of gradient-structured copper. *Mater Trans* 61:708–717. <https://doi.org/10.2320/matertrans.MT-M2019373>
- [13] Wang YM, Ma E (2004) Three strategies to achieve uniform tensile deformation in a nanostructured metal. *Acta Mater* 52:1699–1709. <https://doi.org/10.1016/j.actamat.2003.12.022>
- [14] Ovid'ko IA, Valiev RZ, Zhu YT (2018) Review on superior strength and enhanced ductility of metallic nanomaterials. *Prog Mater Sci* 94:462–540. <https://doi.org/10.1016/j.pmatsci.2018.02.002>
- [15] Meyers MA, Xu YB, Xue Q, Pérez-Prado MT, McNelley TR (2003) Microstructural evolution in adiabatic shear localization in stainless steel. *Acta Mater* 51:1307–1325. [https://doi.org/10.1016/S1359-6454\(02\)00526-8](https://doi.org/10.1016/S1359-6454(02)00526-8)
- [16] Hines J, Vecchio K (1997) Recrystallization kinetics within adiabatic shear bands. *Acta Mater* 45:635–649
- [17] Xu YB, Zhong WL, Chen YJ, Shen LT, Liu Q, Bai YL, Meyers MA (2001) Shear localization and recrystallization in dynamic deformation of 8090 Al–Li alloy. *Mater Sci Eng A* 299:287–295. [https://doi.org/10.1016/S0921-5093\(00\)01412-X](https://doi.org/10.1016/S0921-5093(00)01412-X)
- [18] Lins JFC, Sandim HRZ, Kestenbach HJ, Raabe D, Vecchio KS (2007) A microstructural investigation of adiabatic shear bands in an interstitial free steel. *Mater Sci Eng A* 457:205–218. <https://doi.org/10.1016/j.msea.2006.12.019>
- [19] Timothy SP (1987) The structure of adiabatic shear bands in metals: a critical review. *Acta Metall* 35:301–306. [https://doi.org/10.1016/0001-6160\(87\)90238-0](https://doi.org/10.1016/0001-6160(87)90238-0)
- [20] Xue Q, Gray GT (2006) Development of adiabatic shear bands in annealed 316L stainless steel: Part I. Correlation between evolving microstructure and mechanical behavior. *Metall Mater Trans A* 37:2435–2446
- [21] Hines JA, Vecchio KS, Ahzi S (1998) A model for microstructure evolution in adiabatic shear bands. *Metall Mater Trans A* 29:191–203. <https://doi.org/10.1007/s11661-998-0172-4>
- [22] Wei Q, Kecskes L, Jiao T, Hartwig KT, Ramesh KT, Ma E (2004) Adiabatic shear banding in ultrafine-grained Fe processed by severe plastic deformation. *Acta Mater* 52:1859–1869. <https://doi.org/10.1016/j.actamat.2003.12.025>
- [23] Liu Y, Cao Y, Mao Q, Zhou H, Zhao Y, Jiang W, Liu Y, Wang JT et al (2020) Critical microstructures and defects in heterostructured materials and their effects on mechanical properties. *Acta Mater* 189:129–144. <https://doi.org/10.1016/j.actamat.2020.03.001>
- [24] Wu X, Jiang P, Chen L, Yuan F, Zhu YT (2014) Extraordinary strain hardening by gradient structure. *Proc Natl Acad Sci* 111:7197–7201. <https://doi.org/10.1073/pnas.1324069111>
- [25] Fang TH, Li WL, Tao NR, Lu K (2011) Revealing extraordinary intrinsic tensile plasticity in gradient nano-grained copper. *Science* 331:1587–1590. <https://doi.org/10.1126/science.1200177>
- [26] Song D, Wang G, Zhou Z, Klu EE, Gao B, Ma A, Wu Y, Sun J et al (2020) Developing a high-strength Al–11Si alloy with improved ductility by combining ECAP and cryorolling. *Mater Sci Eng A* 773:138880. <https://doi.org/10.1016/j.msea.2019.138880>
- [27] Calcagnotto M, Ponge D, Demir E, Raabe D (2010) Orientation gradients and geometrically necessary dislocations in ultrafine grained dual-phase steels studied by 2D and 3D EBSD. *Mater Sci Eng A* 527:2738–2746. <https://doi.org/10.1016/j.msea.2010.01.004>
- [28] Jiang J, Britton TB, Wilkinson AJ (2013) Measurement of geometrically necessary dislocation density with high resolution electron backscatter diffraction: effects of detector binning and step size. *Ultramicroscopy* 125:1–9. <https://doi.org/10.1016/j.ultramic.2012.11.003>
- [29] Song D, Wang G, Yang F, Chen H, Liang N, Ma H, Jiang J, Ma X (2020) Microstructure and deformation behavior of a novel steel rebar: Effect of the heterogeneous microstructure of soft ferrite and Hard bainite. *J Mater Res Technol* 9:12281–12292. <https://doi.org/10.1016/j.jmrt.2020.08.085>
- [30] Tao N, Wang Z, Tong W, Sui M, Lu J, Lu K (2002) An investigation of surface nanocrystallization mechanism in Fe induced by surface mechanical attrition treatment. *Acta Mater* 50:4603–4616
- [31] Sun JL, Trimby PW, Yan FK, Liao XZ, Tao NR, Wang JT (2014) Shear banding in commercial pure titanium deformed

- by dynamic compression. *Acta Mater* 79:47–58. <https://doi.org/10.1016/j.actamat.2014.07.011>
- [32] Miszczyk MM, Paul H (2015) Cube texture formation during the early stages of recrystallization of Al-1%wt. Mn and AA1050 aluminium alloys. *IOP Conf Ser Mater Sci Eng* 89:012036. <https://doi.org/10.1088/1757-899x/89/1/012036>
- [33] Miszczyk MM, Paul H, Driver JH (2016) TEM and SEM analyses of the orientation relations of recrystallized grains in a stable Al-1wt.%Mn single crystal. *Mater Charact* 112:68–80. <https://doi.org/10.1016/j.matchar.2015.12.007>
- [34] Mahajan S (2013) Critique of mechanisms of formation of deformation, annealing and growth twins: face-centered cubic metals and alloys. *Scripta Mater* 68:95–99. <https://doi.org/10.1016/j.scriptamat.2012.09.011>
- [35] Zhu YT, Liao XZ, Wu XL (2012) Deformation twinning in nanocrystalline materials. *Prog Mater Sci* 57:1–62. <https://doi.org/10.1016/j.pmatsci.2011.05.001>
- [36] Armstrong RW, Zerilli FJ (1994) Dislocation mechanics aspects of plastic instability and shear banding. *Mech Mater* 17:319–327. [https://doi.org/10.1016/0167-6636\(94\)90069-8](https://doi.org/10.1016/0167-6636(94)90069-8)
- [37] Prinz FB, Argon AS (1984) The evolution of plastic resistance in large strain plastic flow of single phase subgrain forming metals. *Acta Metall* 32:1021–1028. [https://doi.org/10.1016/0001-6160\(84\)90004-X](https://doi.org/10.1016/0001-6160(84)90004-X)
- [38] Chan HL, Ruan HH, Chen AY, Lu J (2010) Optimization of the strain rate to achieve exceptional mechanical properties of 304 stainless steel using high speed ultrasonic surface mechanical attrition treatment. *Acta Mater* 58:5086–5096. <https://doi.org/10.1016/j.actamat.2010.05.044>
- [39] Luo ZP, Zhang HW, Hansen N, Lu K (2012) Quantification of the microstructures of high purity nickel subjected to dynamic plastic deformation. *Acta Mater* 60:1322–1333. <https://doi.org/10.1016/j.actamat.2011.11.035>
- [40] Li Y, Li L, Nie J, Cao Y, Zhao Y, Zhu Y (2017) Microstructural evolution and mechanical properties of a 5052 Al alloy with gradient structures. *J Mater Res* 32:4443–4451. <https://doi.org/10.1557/jmr.2017.310>
- [41] Wright TW, Walter JW (1987) On stress collapse in adiabatic shear bands. *J Mech Phys Solids* 35:701–720. [https://doi.org/10.1016/0022-5096\(87\)90051-2](https://doi.org/10.1016/0022-5096(87)90051-2)
- [42] Yu T, Hughes DA, Hansen N, Huang X (2015) In situ observation of triple junction motion during recovery of heavily deformed aluminum. *Acta Mater* 86:269–278. <https://doi.org/10.1016/j.actamat.2014.12.014>
- [43] Lu K (2014) Nanomaterials. Making strong nanomaterials ductile with gradients. *Science* 345:1455–1456. <https://doi.org/10.1126/science.1255940>
- [44] Zhu Y, Wu X (2019) Perspective on hetero-deformation induced (HDI) hardening and back stress. *Mater Res Lett* 7:393–398. <https://doi.org/10.1080/21663831.2019.1616331>
- [45] Zhu Y, Ameyama K, Anderson PM, Beyerlein IJ, Gao H, Kim HS, Lavernia E, Mathaudhu S et al (2021) Heterostructured materials: superior properties from heterozone interaction. *Mater Res Lett* 9:1–31. <https://doi.org/10.1080/21663831.2020.1796836>
- [46] Ma E, Zhu T (2017) Towards strength–ductility synergy through the design of heterogeneous nanostructures in metals. *Mater Today* 20:323–331. <https://doi.org/10.1016/j.mattod.2017.02.003>
- [47] Yuan F, Yan D, Sun J, Zhou L, Zhu Y, Wu X (2019) Ductility by shear band delocalization in the nano-layer of gradient structure. *Mater Res Lett* 7:12–17. <https://doi.org/10.1080/21663831.2018.1546238>
- [48] Wang YF, Huang CX, He Q, Guo FJ, Wang MS, Song LY, Zhu YT (2019) Heterostructure induced dispersive shear bands in heterostructured Cu. *Scripta Mater* 170:76–80. <https://doi.org/10.1016/j.scriptamat.2019.05.036>

Publisher's Note Springer Nature remains neutral with regard to jurisdictional claims in published maps and institutional affiliations.

Springer Nature or its licensor (e.g. a society or other partner) holds exclusive rights to this article under a publishing agreement with the author(s) or other rightsholder(s); author self-archiving of the accepted manuscript version of this article is solely governed by the terms of such publishing agreement and applicable law.